

Georg Brösigke, Jens-Uwe Repke, Reinhard Schomäcker, Sebastian Matera

The closer the better? Theoretical assessment of the impact of catalytic site separation for bifunctional core–shell catalyst particles

Open Access via institutional repository of Technische Universität Berlin

Document type

Journal article | Accepted version

(i. e. final author-created version that incorporates referee comments and is the version accepted for publication; also known as: Author's Accepted Manuscript (AAM), Final Draft, Postprint)

This version is available at

<https://doi.org/10.14279/depositonce-16119>

Citation details

Brösigke, G., Repke, J.-U., Schomäcker, R., & Matera, S. (2022). The closer the better? Theoretical assessment of the impact of catalytic site separation for bifunctional core–shell catalyst particles. In *Chemical Engineering Journal* (Vol. 446, p. 136891). Elsevier BV. <https://doi.org/10.1016/j.cej.2022.136891>.

Terms of use

 This work is licensed under a Creative Commons Attribution-NonCommercial- NoDerivatives 4.0 International license: <https://creativecommons.org/licenses/by-nc-nd/4.0/>

The Closer the Better? Theoretical Assessment of the Impact of Catalytic Site Separation for Bifunctional Core-Shell Catalyst Particles*

Georg Brösigke^{a,*}, Jens-Uwe Repke^a, Reinhard Schomäcker^b, Sebastian Matera^{c,d}

^a *Process Dynamics and Operations Group, Technische Universität Berlin, KWT9, Straße des 17. Juni 135, 10623 Berlin, Germany*

^b *Institute of Chemistry, Technical Chemistry, Technische Universität Berlin, TC8, Straße des 17. Juni 124, 10623 Berlin, Germany*

^c *Theory Department, Fritz Haber Institute of the Max Planck Society, Faradayweg 4-6, 14195 Berlin, Germany*

^d *Institute for Mathematics, Freie Universität Berlin, Arnimallee 9, 14195 Berlin, Germany*

Abstract

One-pot heterogeneous catalysis with different active centers offers great potential for increasing yield and selectivity. In this field, the distance between the different catalytically active centers starts playing a role and its influence as well as its control is an open question. Here, porous core-shell particles provide the opportunity to control the distance on a mesoscopic scale, where the centers are placed on different shells and are separated by an inert porous matrix. We present a continuum-mechanical model of such particles and exploit symmetry to arrive at a computationally efficient reduced model. Using methanol synthesis from CO₂ on the first kind of center followed by a dimethylether synthesis on a second kind of center as an example, we investigate the influence of the distance between these two centers. In particular, we consider three simple backcoupling mechanisms and address the question whether it is best to place the centers as close as possible or at a non-zero optimal distance. We find that this question can not a priori be answered but the answer depends largely on the employed backcoupling mechanism.

Keywords: core-shell particles, tandem catalysis, reduced modeling, active site distance, mass transfer

*This is the Accepted Manuscript of: Brösigke, G., Repke, J.-U., Schomäcker, R. & Matera, S. (2022). The closer the better? Theoretical assessment of the impact of catalytic site separation for bifunctional core-shell catalyst particles. *Chemical Engineering Journal*, 446, 136891. <https://doi.org/10.1016/j.cej.2022.136891>.

This work is licensed under a Creative Commons Attribution-NonCommercial-NoDerivatives 4.0 International License, <http://creativecommons.org/licenses/by-nc-nd/4.0/>.

*Corresponding author

Email addresses: georg.broesigke@tu-berlin.de (Georg Brösigke), j.repke@tu-berlin.de (Jens-Uwe Repke), schomaecker@tu-berlin.de (Reinhard Schomäcker), matera@fhi-berlin.mpg.de (Sebastian Matera)

Nomenclature

Abbreviations

CMPs	conjugated microporous polymers
CSTR	continuously stirred tank reactor
COFs	metal-organic frameworks
Da	Danköhler Number
DME	dimethylether
DS	dummy species
FBR	fixed bed reactor
MeOH	methanol
MOFs	metal-organic frameworks
RWGS	reverse water gas shift

Greek Symbols

α	sensitivity factor
γ	tortuosity
δ	distance of catalytic shells
ϵ	energy flux, $\text{J m}^{-2} \text{s}^{-1}$
ε	porosity
κ	thermal conductivity, $\text{W m}^{-1} \text{K}^{-1}$
ϕ	sphere coordinate
σ	integral particle production rate, kg s^{-1}
θ	sphere coordinate
Θ	adsorption coverage

τ	production rate, $\text{kg s}^{-1} \text{m}^{-2}$
π	Ludolph's number
ψ	energy flow, W
Ω	subvolume

Latin Symbols

a	solution coefficient
A	active site density, $\text{kg}_{\text{cat}} \text{m}^{-2}$
b	solution coefficient
c	solution coefficient
C	concentration, mol m^{-3}
d	solution coefficient
D	diffusion coefficient, $\text{m}^2 \text{s}^{-1}$
\mathbf{e}_r	radial unit vector
F	flow, kg s^{-1} or mol s^{-1}
h	specific enthalpy, J mol^{-1}
\mathbf{j}	molar flux, $\text{mol m}^{-2} \text{s}^{-1}$
J	coefficient matrix
k	kinetic parameter, various units
K	equilibrium parameter, various units
K	number of particles
L	number of reactions
m	molar mass, kg mol^{-1}
M	number of subvolumes
\mathbf{n}	normal vector

N	number of species	m	spherical harmonics index
p	pressure, bar	p	parameter index
r	radial coordinate, m		
r_l	turnover frequency function, $\text{mol kg}_{\text{cat}}^{-1} \text{s}^{-1}$		
R	radius, m		
R	universal gas constant, $\text{J mol}^{-1} \text{K}^{-1}$		
S	singular surface		
S	selectivity		
T	temperature, K		
x	mole fraction, %		
X	conversion		
y	mass fraction		
Y	spherical harmonics		
Y	yield		
Z	selectivity		
z	vector of unknown variables		

Indices

ξ	subvolume
i	species
j	species
k	particle
l	reaction
l	spherical harmonics index

Superscripts

act.	activation
gas	gas phase
in	entering reactor
kg	mass based
mol	mole based
P	pore
reac.	reaction
+	dimensionless

1. Introduction

With the world’s growing demand for high value chemical products and the need to transform chemical process industry to be based on sustainable resources, new heterogeneous catalysts and concepts need to be developed to achieve an economically and resource efficient operation [1]. One promising approach to increase catalyst efficiency is multifunctional (or one-pot) catalysis, where multiple different active centers within the same reaction chamber conduct different catalytic sub-cycles of a target conversion process [2]. An open question in this field is how the distance between the active sites influences the catalytic efficiency [3]. Intuitively, one might think "the closer the better", and the intimacy criterion [4] was employed for justification [5, 6]. However, there are prominent examples where this rule does not apply [2, 7, 8] and there is therefore the need to control the distance.

One approach to control the proximity on the mesoscale are catalytic core-shell particles [9, 10], which can outperform monofunctional catalysts when designed properly [11]. In the bifunctional case, those incorporate two different active sites, one located at the inner core, one located at the outer shell. Between both catalytically active layers, a porous, inert matrix (e.g. zeolites, MOFs, COFs or CMPs) can be placed to separate both catalytically active sites [12]. For this matrix to have an effect, intraparticle transport phenomena must play a key role for the interaction of the two catalysts. Understanding of these effects is crucial for a proper design of such catalyst particles, which is not yet the case. A methodology for the synthesis of mesoscale core-shell particles has been established that allows for tuning of essential structural parameters [13]. This allows to separately adjust the catalyst loading of core and shell as well as the size of the different parts of the particles. The variety of synthesis parameters requires a rational design of such catalysts for their optimal performance.

We present a continuum mechanical model for coupled reaction and transport processes in such core-shell particles with two different catalytically active centers. We exploit the typically weak concentration dependence of diffusion coefficients as well as symmetry to reduce the resulting set of non-linear coupled partial differential equations to a set of just a few algebraic equations. This allows for an efficient coupling of the particle model to macroscopic reactor models. As a showcase, we employ a Continuously Stirred Tank Reactor (CSTR) model and bifunctional particles for the synthesis of dimethylether (DME) from CO_2 and hydrogen. These particles consist of a $\text{CuO}/\text{ZnO}/\text{Al}_2\text{O}_3$ catalyst at the core for the synthesis of methanol (MeOH) and H-ZSM-5 zeolite catalyst at the outer shell for the conversion of MeOH to DME. A similar kind of model for core-shell particles with the same combination of catalysts has already been investigated in a previous study [14] , however, with a different focus. Our particle model primarily differs from that

employed in ref. [14] in that we allow for a separating inert matrix and that we model the H-ZSM-5 as a singular surface. On the one hand, this allowed for the reduction to an algebraic set of equation, in contrast to the differential equation model in ref. [14] . Thereby, we significantly increased the computational efficiency. On the other hand, this reduces the complexity such that a detailed discussion of the influence of the distance and the transport does not become overly involved. In summary, the existing model [14] might be more accurate but the proposed model should be better suited for numerical optimization in regards of catalyst loading and core-shell distance. Also, the existing model will be more accurate for thick shells of H-ZSM-5 around the core. Our model instead targets at those recent developments in synthesis, where the two catalysts are deposited in thin shells and separated by an inert porous matrix [13]. In such cases the modeling of both catalytically active domain as singular surfaces is well justified.

Whether the modeling of the catalytic shells as singular surfaces or extended domains is appropriate, depends on the employed catalysts, shell thickness, transport properties of the shells etc. and, of course, the research question. For the purpose of this study, we find that this basic assumption is well justified, because we target at a qualitative understanding and use a model system instead of a quantitative model of some real life experiment. With our reduced model, we investigate whether there is a non-zero optimal distance where conversion or selectivity gets maximized. We particularly focus on the influence of a possible backcoupling due to the possibility that DME interacts with the MeOH synthesis catalysts. This is an aspect, which is not present when conducting both steps sequentially in two different chambers and which, therefore, is not accounted for in the employed of-the-shelf kinetic models for CuO/ZnO/Al₂O₃[15] and H-ZSM-5 [16]. To discuss this, we introduce three simple backcoupling mechanisms: i) no backcoupling, i.e. DME does not even adsorb on CuO/ZnO/Al₂O₃, ii) poisoning of CuO/ZnO/Al₂O₃ by DME using Langmuir adsorption, and iii) DME undergoing a reaction to an unwanted side product on CuO/ZnO/Al₂O₃. Another possible interaction of the two reactions, the adsorption of water at the ZSM-5 will not be considered here, because it causes no side product but only an inhibition of the active sites of the second catalytic conversion since it will not be possible to distinguish between the impact of the produced water from both reactions.

We find that for i) and ii) the optimal distance is actually zero, with the only difference that the poisoning lowers the conversion. If we allow DME to undergo a side reaction the optimal distance instead is non-zero. To shine light into this, we have conducted a sensitivity analysis (cf. Appendix B) in a generalization of the concept of the Degree of Rate Control known from reaction kinetics for the determination of rate-determining steps. Depending on the distance, the activity is controlled by an interplay of transport and kinetics and the maximum of case iii) is characterized by a change of the dominant controlling factors, where, for small

distances, the side reaction and the transport of its product have a large negative impact which vanishes for distances larger than the optimum.

2. Theory and model details

In this study, we want to consider a reaction chamber packed with the afore mentioned core-shell particles and gaseous reactants and products. Because of the typical large differences between particle size and reactor volume, this intrinsically is a multiscale problem. In Fig. 1, the schematic assembly of a reactor filled with catalyst particles is shown together with the phenomena taking place at different scales [17]. On the largest, the device scale, we have the conditions at the inlet, total flow and heat provided to the reactor and the reactor response, i.e. the concentrations of the reactants and products at the outlet. On a smaller scale, we consider the coarse distribution of species in the chamber. That is we divide the chamber into subvolumes, each of which typically still contains a large number of particles, and look at the amount of each species in each subvolume. Looking closer at these subvolumes, on scale of multiple particles, we actually resolve the concentration and transport of the gas around the individual particles. Generally, there might be gradients in the surrounding gas phase, but, on the scale of the particle diameter, transport is dispersion controlled and the surrounding gas can often be assumed homogeneous. Finally, we have diffusion and reaction within a single core-shell particle. In this study, we consider particles which primarily consist of porous inert material. Catalysts material is only present in thin concentric shells around the origin of the particle. Because transport can be much slower in a porous material than in a gas, significant concentration gradients can build up within a single particle and must be accounted for.

We derive a simple model to describe the coupled kinetics and transport in spherical particles and employ established empirical rate expressions. We couple this to a reactor model using a continuously stirred tank reactor (CSTR) as an example, where the extension to more complex reactor models is straightforward. In principle, this multiscale approach could also be extended to incorporate even quantum-chemical scales by adapting the approach presented in ref. [18] .

Our reduced particle model relies on four assumptions. First, there is the mentioned homogeneity of the surrounding gas phase on the particle scale, such that a particle experiences the same gas phase conditions over its whole surfaces. Whether or not this is a valid assumption depends on the particle size and the reactor setup, such as geometry and flow rate, but, for larger particles, also the general activity of the particles. Further, we will exploit spherical symmetry, which, of course, is an idealization, and depends on the catalyst preparation. We will model the catalytic shells as singular surfaces, which requires that the

composition and temperature within a shell shows negligible variations in normal (radial) direction. This depends on the nature and amount of the catalyst in the shell as well as the transport through it. This is a common (implicit) assumption in reactor modeling of catalysts supported on (non-porous) particles. Finally, we neglect any spatial and concentration/temperature dependence of the transport coefficients and the specific enthalpies in the inert layers between the active shells. Considering the high sensitivity of kinetic models on concentration and temperature and the typical large uncertainty, this can be considered a rather weak assumption. For the coupling of the particle model to the reactor model, we will further assume that all particles are identical. While not absolutely necessary, this leads to a particularly efficient hybrid model.

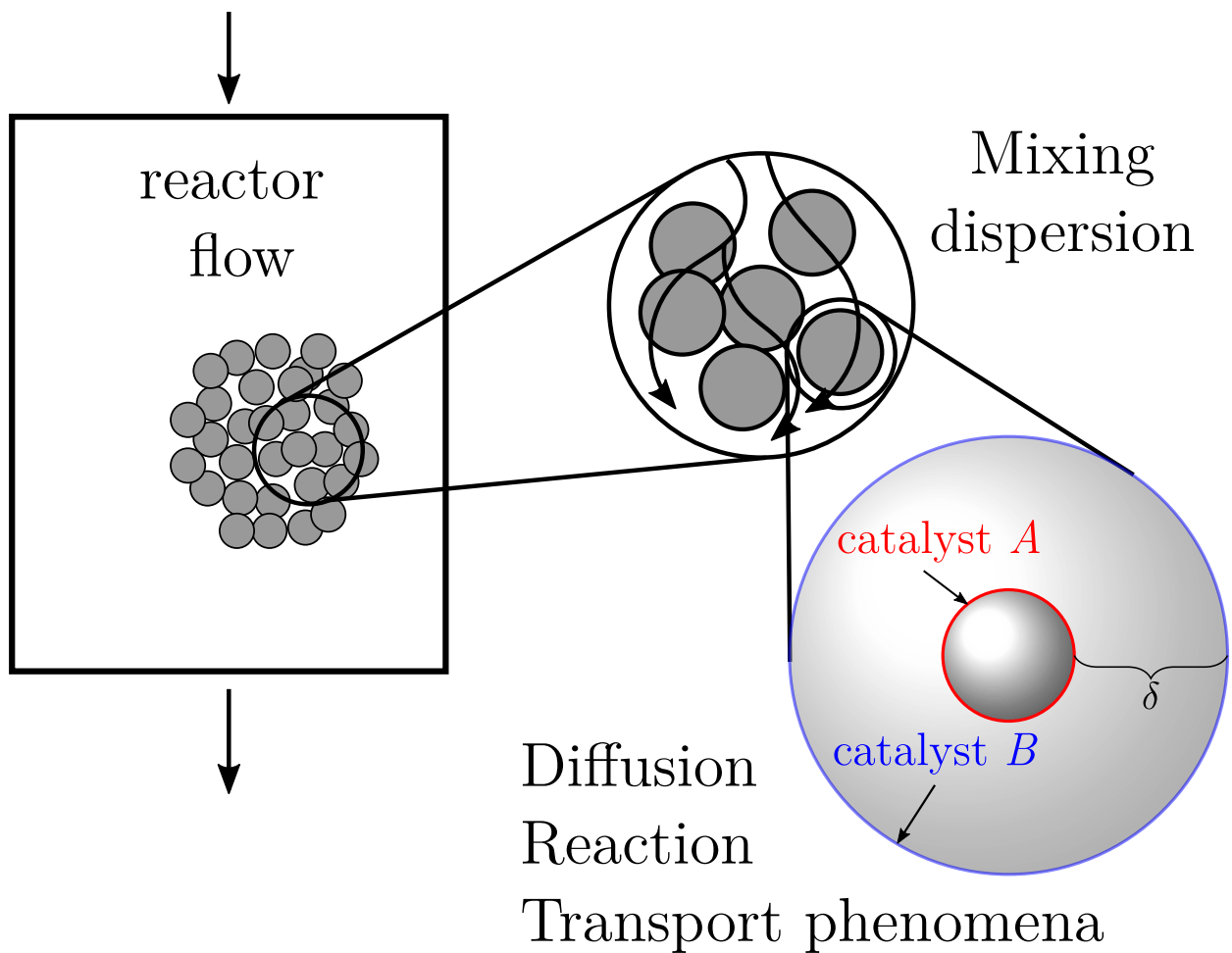


Figure 1: Different transport phenomena in generic reactor filled with catalyst on different scales, adapted from [17]

2.1. Core-Shell Model

We consider the transport and reaction of N species in a spherical porous particle of radius R and, therefore, we work in spherical coordinates (r, ϕ, θ) . We assume that the solid matrix is at rest and rigid.

Reactions happen only within singular surfaces S_ξ located at $0 < R_1 < \dots < R_\xi < R_M = R$ and we use the convention that the normal vector on these surfaces is the unit vector \mathbf{e}_r pointing in r -direction. These decompose the volume of the particle into M subvolumes $\Omega_\xi = \{(r, \phi, \theta) | R_{\xi-1} < r < R_\xi\}$, where we used the convention $R_0 = 0$. We assume that within Ω_ξ all fields are twice differentiable and a superscript (ξ) is used to distinguish the field values within the subdomains. We use the convention that $\xi = M + 1$ denotes the gas phase surrounding the particle.

A sketch of such a core-shell particle with two active layer S_1 and S_2 is shown In Fig. 2.

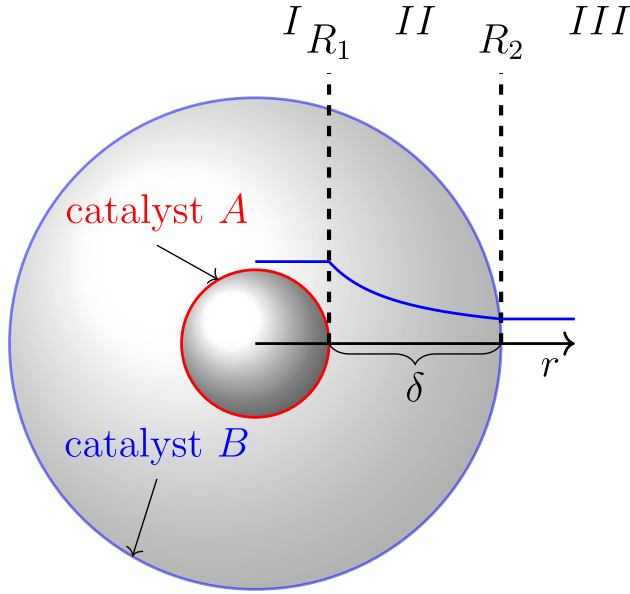


Figure 2: Sketch of representative particle with two reactive shells. The inner shell located at R_1 represents catalyst A (here Cu/ZnO), the outer shell at R_2 represents catalyst B (here ZSM-5). Region I: Core, no transport; Region II: porous support, Knudsen Diffusion; Region III: surrounding gas phase (here CSTR-behavior)

2.1.1. Inert Porous Medium

The starting point for our particle model are the balance equations the species' mass at steady state for the subvolumes Ω_ξ , $\xi \in [1, M]$ of the single particle, which are filled with a catalytically inactive porous material. For simplicity, we assume that species transport within Ω_ξ is governed by Knudsen diffusion, i.e. we have for the mass flux $\mathbf{j}_i^{(\xi)}$ of the i -th species $\mathbf{j}_i = -m_i D_i^{(\xi)} \nabla C_i^{(\xi)}$, where m_i is the mass of a molecule of species i , $D_i^{(\xi)}$ is diffusion coefficient and $C_i^{(\xi)}$ is the molar concentration. (Intrinsic) heat conduction is assumed to obey Fourier's law and the total energy flux $\boldsymbol{\epsilon}$ is then $\boldsymbol{\epsilon} = \nabla \kappa^{(\xi)} \cdot T^{(\xi)} - \sum_{i=1}^N h_i D_i^{(\xi+1)} \nabla C_i$, where κ is the thermal conductivity and h_i is the specific enthalpy. The steady state balance equations for the bulk (within Ω_ξ) read then

$$\text{species balance: } \nabla \cdot m_i D_i^{(\xi)} \nabla C_i^{(\xi)} = 0, \quad (1)$$

$$\text{energy balance: } \nabla \cdot \kappa^{(\xi)} \nabla T^{(\xi)} + \sum_{i=1}^N \nabla \cdot h_i^{(\xi)} D_i^{(\xi)} \nabla C_i^{(\xi)} = 0, \quad (2)$$

where the zero on the right hand side of eqn. (1) and (2) results from the fact that we neglected direct reactions of gas phase species and the assumed the porous matrix to be inactive and further neglected radiative heat transfer.

2.1.2. Singular surfaces

The transport equations of the different inert domains (1) and (2) are connected by jump conditions at the reactive singular surfaces S_ξ , $\xi \in [1, M]$. For this, we utilize the balance equations for singular surfaces [19] and neglect tangential transport within the surface, as it is common in reactive flow modeling of catalytic processes [20]. Further, we employ the requirement that concentrations and temperature are continuous across the singular surfaces. This requirement is reasonable considering that the catalytic shells are assumed to be rather thin and, therefore, no significant normal variations can build up within a shell. For the $M - 1$ inner shells, this leads to the equations on S_ξ , $\xi \in [1, M - 1]$

$$\text{continuity species: } C_i^{(\xi)} = C_i^{(\xi+1)}, \quad (3)$$

$$\text{continuity temperature: } T^{(\xi)} = T^{(\xi+1)}, \quad (4)$$

$$\text{species balance: } -[m_i D_i^{(\xi)} \nabla C_i^{(\xi)} - m_i D_i^{(\xi+1)} \nabla C_i^{(\xi+1)}] \cdot \mathbf{n} = \tau_i^{(\xi)}, \quad (5)$$

$$\text{energy balance: } [\kappa^{(\xi)} \nabla T^{(\xi)} + \sum_{i=1}^N h_i^{(\xi)} D_i^{(\xi)} \nabla C_i^{(\xi)} - \kappa^{(\xi+1)} \nabla T^{(\xi+1)} - \sum_{i=1}^N h_i^{(\xi+1)} D_i^{(\xi+1)} \nabla C_i^{(\xi+1)}] \cdot \mathbf{n} = 0 \quad (6)$$

where $\tau_i^{(\xi)}$ is the rate of production of species i in the shell ξ and \mathbf{n} is the normal vector pointing into $\Omega_{\xi+1}$. The left hand sides of (5) and (6) represent the flux of species and energy into S_ξ and this must balance with the production terms on the right hand sides.

We assume that we have L chemical reactions each having its own intrinsic turnover frequency function $r_l(C_i, T)$, returning the number of reactions per time and active site. For generality, we assume that each reaction can have its own type of active site. In this way, we also distinct two reactions with the same

stoichiometry but appearing nanoscopically at different active sites, e.g. on different catalyst materials or terminations. We assume that, nanoscopically, the different catalyst particles within a singular surface see the same partial pressures and temperature and that these equal the continuum level partial (pore) pressure and temperature. Then, we can write

$$\tau_i^{(\xi)} = m_i \sum_{l=1}^L \nu_{i,l} A_l^{(\xi)} r_l(C_i^{(\xi)}, T^{(\xi)}) \quad (7)$$

where $\nu_{i,l}$ is the stoichiometric coefficient and $A_l^{(\xi)}$ is the number of active sites of the reaction l in the surface S_ξ per unit surface area.

For the remaining surface S_M , i.e. the interface between the particle and the surrounding gas phase, we again assume continuity of temperature and concentrations

$$\text{continuity species: } C_i^{(M)} = C_i^{(M+1)} \quad (8)$$

$$\text{continuity temperature: } T^{(M)} = T^{(M+1)} \quad (9)$$

where, as introduced, $T^{(M+1)}$ and $C_i^{(M+1)}$ are the temperature and concentrations in the surrounding gas phase. If these are given, eqn. (1) to (9) form a closed set of equations from which we can determine concentrations and temperature within the particle. In reality, $T^{(M+1)}$ and $C_i^{(M+1)}$ will not explicitly be known, but will need to be determined from a reactor model. Species and energy balances for singular surface will then serve for coupling the particle with the reactor model, in a similar fashion as eqn. (5) and (6). In this study, we will consider coarse-grained reactor models, where we do not resolve every particle. For such models, coupling will be done using the net rate of species and heat production of a single particle. The rate of net species production σ_i is given by

$$\sigma_i = \int_{S_M} \tau_i^{(M)} + (m_i D_i^{(M)} \nabla C_i^{(M)}) \cdot \mathbf{n} dA \quad (10)$$

which is nothing than the integrated mass flux of species i from the gas phase into the reactive interface between particle and surrounding gas phase. Analogously, the rate of heat productions is the integral energy flux ψ into the reactive interface and is given by

$$\psi = \int_{S_M} [-\kappa^{(M)} \nabla T^{(M)} - \sum_{i=1}^N h_i^{(M)} D_i^{(M)} \nabla C_i^{(M)}] \cdot \mathbf{n} dA \quad (11)$$

. For our reactor model, we will later assume isothermal operation, such that the heat production will not further be needed.

2.1.3. Model reduction

Given $T^{(M+1)}$ and $C_i^{(M+1)}$, Eqn. (1) to (9) is a closed set of equations which we could use to determine the unknowns $C_i^{(\xi)}$ and $T^{(\xi)}$. However, being a set of coupled partial differential equations with nonlinear jump conditions, their numerical solution is computationally very demanding. We therefore introduce two reasonable simplifications to arrive at a computationally cheap model, which still captures the main effects.

The first simplification is build upon the observation that eqn. (1) and (2) were linear if $D_i^{(\xi)}$, $\kappa^{(\xi)}$ and $h_i^{(\xi)}$ were independent of $C_i^{(\xi)}$ and $T^{(\xi)}$. For instance, they might be given by their values for the applied concentrations and temperature and we will employ this simplification. This assumption is rather well founded as $D_i^{(\xi)}$, $\kappa^{(\xi)}$ and $h_i^{(\xi)}$ typically only weakly depend on $C_i^{(\xi)}$ and $T^{(\xi)}$; especially compared to r_l , which usually depends sensitively on both. If we further restrict to those cases where the porous medium has spatially homogeneous transport properties within each subvolume Ω_ξ , $D_i^{(\xi)}$, $\kappa^{(\xi)}$ and $h_i^{(\xi)}$ are simply constant in Ω_ξ (but might differ in value between different subvolumes). The system of partial differential equations (1) and (2) has then the shape $\underline{J}^{(\xi)} \Delta \underline{z}^{(\xi)} = 0$. Here, $\underline{z}^{(\xi)} = (C_1^{(\xi)}, \dots, C_N^{(\xi)}, T^{(\xi)})^T$ and the coupling matrix $J^{(\xi)}$ has the entries $J_{i,j}^{(\xi)} = D_i^{(\xi)} \delta_{i,j}$ for $i, j \in [1, N]$, $J_{i,N+1}^{(\xi)} = 0$ for $i \in [1, N]$, $J_{N+1,i}^{(\xi)} = h_i^{(\xi)} D_i^{(\xi)}$ for $i \in [1, N]$, and $J_{N+1,N+1}^{(\xi)} = \kappa^{(\xi)}$. The matrix J is invertible and we can rewrite the system (1) and (2) as $\Delta C_i^{(\xi)} = 0$ and $\Delta T^{(\xi)} = 0$. This means that $C_i^{(\xi)}$ and $T^{(\xi)}$ must be in the null space of the Laplace operator Δ . They can thus be represented as a superposition of regular and irregular solid harmonics[21], i.e. in spherical coordinates (r, ϕ, θ)

$$C_i^{(\xi)}(r, \phi, \theta) = \sum_{l=0}^{\infty} \sum_{m=-l}^{+l} (a_{i,lm}^{(\xi)} r^l + b_{i,lm}^{(\xi)} \frac{1}{r^{l+1}}) Y_{lm}(\phi, \theta) \quad (12)$$

$$T^{(\xi)}(r, \phi, \theta) = \sum_{l=0}^{\infty} \sum_{m=-l}^{+l} (c_{i,lm}^{(\xi)} r^l + d_{i,lm}^{(\xi)} \frac{1}{r^{l+1}}) Y_{lm}(\phi, \theta) \quad (13)$$

where $Y_{lm}(\phi, \theta)$ are the spherical harmonics. Any choice of the expansion coefficients $a_{i,lm}^{(\xi)}$, $b_{i,lm}^{(\xi)}$, $c_{i,lm}^{(\xi)}$ and $d_{i,lm}^{(\xi)}$ solves eqn. (1) and (2) and they are only determined by the jump conditions in eqns. (3) - (9). The problem has thus be reduced from three dimensions to a problem on the two-dimensional singular surfaces.

The second step is to additionally restrict to spherical symmetric particles. The homogeneity of the surrounding gas phase then implies that also $C_i^{(\xi)}(r, \phi, \theta)$ and $T^{(\xi)}(r, \phi, \theta)$ are independent of the angles ϕ

and θ , if we place the origin at the center of the particle. Since all spherical harmonics except for Y_{00} depend on the angles, all expansion coefficients except $a_{i,00}^{(\xi)}$, $b_{i,00}^{(\xi)}$, $c_{i,00}^{(\xi)}$ and $d_{i,00}^{(\xi)}$ must be identical zero. Further, $b_{i,00}^{(1)} = 0$ and $d_{i,00}^{(1)} = 0$, because else the fields would be singular at the origin. A more physical explanation is that else every spherical subvolume of Ω_1 around the origin, would see either a net gain or loss of species and energy. Without sources or sinks in this subvolume, this would contradict stationarity. The particle model thus reduces to an algebraic set of equations with $O(MN)$ unknown coefficients.

2.2. Reactor model

The particle model must be complemented with a reactor model for the treatment of the surrounding gas. In principle, it is possible to simulate the detailed gas transport around the particles using Computational Fluid Dynamics and couple particle models as ours to it [22]. However, such approaches are computationally demanding already for a small number of particles. When the particles become small and their number grows, these approaches become unfeasible. Therefore, coarse-grained models are much more widespread, where a volume element contains a large number of particles. These are not explicitly resolved, but only their cumulative action is considered and the gas is assumed to be homogeneous within a volume element.

Here, we employ the simplest of such coarse-grained models, an isothermal and isobaric Continuously Stirred Tank Reactor. That is, we do not only assume homogeneous concentrations within a volume element but within the whole reaction chamber. The temperature $T^{(M+1)}$ at the particles' surfaces is then simply given by the preset bulk gas temperature T^{gas} . The stationary species mass balance for this type of reactor model with K core-shell particles is given by

$$F^{\text{kg,in}}(y_i^{\text{in}} - y_i^{(M+1)}) + \sum_{k=1}^K \sigma_{k,i} = 0 \quad (14)$$

where $F^{\text{kg,in}}$ is the total applied mass flow and y_i^{in} is the applied mass fraction of the i -th species. $y_i^{(M+1)}$ is the mass fraction of the i -th species in the chamber. The incoming mass flux $F^{\text{kg,in}}y_i^{\text{in}}$ and the outgoing mass flux $F^{\text{kg,in}}y_i^{(M+1)}$ of species i must balance with the total production of that species by the core-shell particles. This is given by the sum of the production rates $\sigma_{k,i}$, given by eq. (10). We want to assume that all particles are identical such that $\sum_{k=1}^K \sigma_{k,i} = K\sigma_i$ and σ_i can thus be determined from a single particle model. The hybrid model then has roughly M times more unknowns (and equations to solve) than a CSTR model with simple single shell particles.

2.3. Computational Implementation

The model was formulated using the in-house model generator tool MOSAICModeling, developed by the Process Dynamics and Operations Group [23]. The model was generically implemented to be able to handle L reactions, N species and M porous and inert subvolumes. The cases presented in this study are limited to $M = 2$ porous and inert subvolumes, resulting in two reactive singular surfaces, but could easily be adapted to different conformations, reactions and species involved. The generic equations are instantiated with the according indices, generating the system of algebraic equations. After defining the parameters, the model is translated and exported to MATLAB® via a native export function of MOSAICModeling. In MATLAB®, the system of algebraic equations is solved with the non-linear solver *fsolve* using the *trust-region-dogleg*-algorithm with a residual control of 1×10^{-12} .

The solution of the nonlinear equation system of the reduced model is calculated within seconds on a single core. The main advantage lies in not having to solve a system of coupled partial differential equations on finite volumes, for which at least a workstation with multiple cores if not a computing cluster would have been necessary. Moreover, the solution is very robust, since no discretization is required.

3. Material and methods

The following section will give an overview of the applied methods and the system we look at in more detail. Firstly, the applied modeling approaches for the chemistry will be presented for each location in Fig. 2, followed by a detailed description of the transport phenomena. As mentioned before, in the scope of this study we will look at bifunctional core-shell catalyst particles, in which two different catalytic active sites are located as can be seen in Fig. 2. At the inner radius R_1 (the core) catalyst A is placed, where the methanol synthesis reaction is promoted. The second catalyst is located at the outer radius R_2 (the shell). Here, catalyst B promotes the dehydration from methanol to dimethylether. We will consider the particles to be operated within a CSTR. We will investigate the influence of different values of the distance between core and shell $\delta = R_2 - R_1$. In all our studies we will keep R_1 and the total amount of mass of both catalysts in the chamber fixed. We employ effective kinetic models of the uncoupled cases from literature for both reactions. In order to address possible backcoupling, we later extend the kinetic model of catalyst A with simple models in order to account for poisoning by DME in a first step and DME conversion in a second step.

3.1. Chemistry

In the following section we will describe the applied modeling approaches as well as simplifications for the chemical reactions at each position in the particle.

Core: Region I marks the core region. Here, no chemical reaction is considered to be taking place. It is assumed that no active sites are located in this region.

Inner surface: At the core's surface R_1 , the first catalytically active layer is located. In this article we will consider catalyst A to be commercially available Cu/ZnO based methanol synthesis catalyst. On that catalyst, we assume the MeOH synthesis ($\text{CO}_2 + 3\text{H}_2 \rightleftharpoons \text{CH}_3\text{OH} + \text{H}_2\text{O}$) and the reverse water gas shift reaction ($\text{CO}_2 + \text{H}_2 \rightleftharpoons \text{CO} + \text{H}_2\text{O}$) to be taking place. The reactions are described by the proposed macrokinetics from [24] with the corrected parameters from [15] with equilibrium constants given by [25].

$$r_{\text{RWGS}} = k_5 \cdot \frac{p_{\text{CO}_2} \cdot \left(1 - \frac{p_{\text{CO}} \cdot p_{\text{H}_2\text{O}}}{p_{\text{H}_2} \cdot p_{\text{CO}_2} \cdot K_{\text{RWGS}}}\right)}{1 + K_2 \cdot \frac{p_{\text{H}_2\text{O}}}{p_{\text{H}_2}} + K_3 \cdot (p_{\text{H}_2})^{0.5} + K_4 \cdot (p_{\text{H}_2\text{O}})} \quad (15)$$

$$r_{\text{MeOH}} = k_1 \cdot \frac{p_{\text{CO}_2} \cdot p_{\text{H}_2} \cdot \left(1 - \frac{p_{\text{H}_2\text{O}} \cdot p_{\text{MeOH}}}{(p_{\text{H}_2})^3 \cdot p_{\text{CO}_2} \cdot K_{\text{MeOH}}}\right)}{\left(1 + K_2 \cdot \frac{p_{\text{H}_2\text{O}}}{p_{\text{H}_2}} + K_3 \cdot (p_{\text{H}_2})^{0.5} + K_4 \cdot (p_{\text{H}_2\text{O}})\right)^3} \quad (16)$$

The kinetic parameters k_p and the equilibrium constants K_p are calculated by Arrhenius' equation

$$k_p = k_{0,p} \cdot \exp\left(\frac{E_p^{\text{act.}}}{R_{\text{gas}} \cdot T}\right) \quad (17)$$

$$K_p = K_{0,p} \cdot \exp\left(\frac{E_p^{\text{reac.}}}{R_{\text{gas}} \cdot T}\right) \quad (18)$$

with the corresponding values for frequency constant $k_{0,p}$ and activation energy $E_p^{\text{act.}}$ and equilibrium parameter $K_{0,p}$ and free energy of reaction $E_p^{\text{reac.}}$ listed in Table C.2 in Appendix C. Analogically to [24], who based their statement on [26] and [27], we assume the direct conversion of CO_2 to be the major path towards methanol.

Inert porous material: Region II marks the porous catalytically inactive support material between the active layers. Here, it is also assumed that no active sites are located.

Outer surface: The outer shell is located in a distance of δ at R_2 , which also represents the overall particle radius. At the particle's surface at R_2 catalyst B is located. In this study, we will consider it to be ZSM-5 for DME dehydration. On that singular surface the dehydration from methanol to dimethylether ($2\text{CH}_3\text{OH} \rightleftharpoons \text{C}_2\text{H}_6\text{O} + \text{H}_2\text{O}$) is implemented according to the macro-kinetic approach from [16] with the

equilibrium constant as described by [28].

$$r_{\text{DME}} = k_6 \cdot (K_7)^2 \cdot \frac{(p_{\text{MeOH}})^2 - \frac{p_{\text{DME}} \cdot p_{\text{H}_2\text{O}}}{K_{\text{DME}}}}{(1 + K_7 \cdot p_{\text{MeOH}} + K_8 \cdot p_{\text{H}_2\text{O}})^2} \quad (19)$$

Reactor: Since we consider the chemical reaction to be exclusively of heterogeneous nature, no reaction is considered in the gas phase on reactor level.

3.2. Transport

In the following section we will describe the applied modeling approaches as well as simplifications for the transport at each position in the particle.

Core: In the region I (the core), no net transport occurs. This is due to the symmetrical shape as discussed before. Eqn. (12) derives to

$$C_i^{(1)}(r \leq R_1) = a_{i,00}^{(1)} Y_{00}. \quad (20)$$

Note, we have allowed the core to be porous, but inert. However, its transport properties have no effect on the model outcome, because all fluxes are zero in steady state and under spherical symmetry. Especially, the core might be non-porous without affecting the results. The result is a constant concentration in steady state, independently from the transport resistance in the core.

Inner surface: The transport at the singular surface is described by Eq. (5).

Inert porous material: In region II (inert support) transport is assumed to be well described by Knudsen Diffusion and the overall species balance Eq. (1). In this study we arbitrarily chose constant values for tortuosity $\gamma = 1.5$, porosity $\varepsilon = 0.5$ and the pore radius $R^P = 1 \times 10^{-8}$ m just for demonstration purpose. The relative findings are not affected. Furthermore, for simplification, the diffusivity coefficients are evaluated at the gas bulk temperature and therefore are constant across r . This can be justified by a very small temperature change in the particle. The temperature at R_1 is less than 0.4 percent lower than at R_2 (cf. Appendix A).

$$D_i = \frac{\varepsilon}{\gamma} \cdot \frac{2 \cdot R^P}{3} \cdot \sqrt{\frac{8 \cdot R^{\text{gas}} \cdot T^{\text{gas}}}{\pi \cdot m_i}} \quad (21)$$

Outer surface: At the very outer surface of the particle, the diffusive fluxes between surrounding gas phase and particle is defined by Eq. (10).

Reactor: The transport on reactor level is described by Eq. (14). Here, only transport based on the macroscopic flow F is considered and the out-going concentrations are determined by the diffusive fluxes $\sigma_{k,i}$ from the particles.

4. Results and discussion

In this study we carried out simulations for three different test cases with increasing complexity. In all cases the inner radius of the core-shell particle R_1 is held constant while the outer radius R_2 is increased and therefore the distance between the catalysts δ is varied. Please note that the catalyst distance was varied in several orders of magnitude (1×10^{-9} m to 1×10^{-3} m). Since the continuum assumption does not necessarily hold for very low δ values, the interpretation for $\delta \leq 1 \times 10^{-7}$ m needs to be done with care. Despite that, we show the whole range to show the asymptotic behavior since for larger diffusivity constant, the limiting behavior in the gray marked region would appear at larger scales where the continuum model would still be valid. Moreover, on the nano-scale other effects like metal ion migration take place which are currently not considered in the model. Nevertheless, for the purpose of this study, the fundamental investigation of the influence of the distance between different catalysts for various backcoupling mechanisms, the developed model produces qualitatively comparable results. The design parameters chosen for all showcases presented in the results are given in Table 1. The variation of the distance between two catalytically active shells is shown for three different cases.

The results will mainly be discussed using the characteristic global properties on reactor scale of the CO₂-conversion X_{CO_2} , the yield Y_i and the selectivity S_i defined as follows:

$$X_{\text{CO}_2} = \frac{y_{\text{CO}_2}^{\text{in}} - y_{\text{CO}_2}^{(M+1)}}{y_{\text{CO}_2}^{\text{in}}} \quad (22)$$

$$Y_i = \frac{y_i^{(M+1)} - y_i^{\text{in}}}{y_{\text{CO}_2}^{\text{in}}} \frac{m_{\text{CO}_2}}{m_i} \frac{\nu_{\text{CO}_2}}{\nu_i} \quad (23)$$

$$S_i = \frac{Y_i}{X_{\text{CO}_2}}, \quad (24)$$

and the dimensionless Damköhler Number is used to quantify the ratio between reaction kinetics and diffusivity.

$$\text{Da}_l = \frac{r_l \cdot \delta \cdot m_l}{D_i \cdot C_i^{\text{gas}} \cdot (R_2)^2} \quad (25)$$

Table 1: Design parameters for simulation study

Name	Parameter	value	unit
T^{gas}	gas bulk temperature	513.15	K
p^{gas}	gas bulk pressure	10	bar
R_1	core radius	1×10^{-4}	m
κ	thermal conductivity	0.17376	$\text{W m}^{-1} \text{K}^{-1}$
ε	porosity	0.5	-
γ	tortuosity	1.5	-
R^{P}	pore radius	1×10^{-8}	m
K	number of particles	1000	-
$F^{\text{kg,in}}$	inlet mass flow	1×10^{-4}	kg s^{-1}
$y_{\text{N}_2}^{\text{in}}$	inlet mass fraction	0.36	-
$y_{\text{H}_2}^{\text{in}}$	inlet mass fraction	0.08	-
$y_{\text{CO}_2}^{\text{in}}$	inlet mass fraction	0.56	-
$F^{\text{mol,in}}$	inlet mole flow	0.006 56	mol s^{-1}
$x_{\text{N}_2}^{\text{in}}$	inlet mole fraction	19.6	%
$x_{\text{H}_2}^{\text{in}}$	inlet mole fraction	61.0	%
$x_{\text{CO}_2}^{\text{in}}$	inlet mole fraction	19.4	%
m_{R_1}	Cu/ZnO catalyst loading	2×10^{-5}	kg
m_{R_2}	ZSM-5 catalyst loading	2×10^{-5}	kg

4.1. Case I - No Coupling ($K_{0,8} = 0$ & $k_{0,9} = 0$)

In the basic case presented here, both reactive surfaces are considered not to be coupled, except for the methanol and the water being relevant in both methanol and dimethylether synthesis. Otherwise, the two shells are not necessarily affected by each other.

On the left axis, Fig. 3 (a) depicts the yield (Eq. (23)) of DME and methanol for showcase I (no coupling) for varying catalyst distance by means of a constant inner radius R_1 and a variable outer radius R_2 . The selectivity towards DME (Eqs. (22) and (24)) is shown on the right axis. Both, yield and selectivity increase with lowering the distance between the two active shells where the active sites are located. By decreasing the catalyst distance, the mass transfer resistance between the shells decreases. Therefore, the educt concentrations for the first reaction (i. e. CO_2 and H_2) are higher at the inner shell, where they are consumed, which, in first place, leads to higher reaction rates. As a consequence of a higher MeOH reaction rate, the concentration at the inner shell increases as well with the flux, since the transport resistance is low for small catalyst distances. This results in a higher methanol flux to the outer shell where the second reaction takes place and benefits from more MeOH being transported here, leading to a higher reaction rate for the DME synthesis reaction. Therefore, for the case without coupling, we see that the closer the catalysts are, the higher the DME yield and its selectivity. Fig. 3 (b) shows the Damköhler Number as defined in Eq. (25) for the reactions involved in showcase I. With increasing distance, Da increases, showing

a distinct maximum at an individual distance for all reactions but generally showing the same developing. The reaction network is controlled by the MeOH synthesis step, as it shows the lowest Da Number of all.

In Fig. 4 the normalized sensitivities of the yield of DME (a) and the yield of MeOH (b) on selected parameters (i. e. reaction rate constants and Knudsen Diffusivity constants) are depicted. The sensitivities have been calculated according the approach outlined in Appendix B. This approach is a generalization of the concept of the Degree of Rate Control to problems beyond mere kinetics.

- $Z_{r_{\text{MeOH}}}$: Increasing the MeOH reaction rate constant leads to a higher yield of DME. This is expected since DME is produced from MeOH. The higher the MeOH production, the larger the educt concentration for the DME synthesis. The amplification decreases for larger distance, due to mass transfer limitation taking over. As r_{MeOH} shows the highest influence on the yield of both DME and MeOH of all reaction rates it can be concluded that this reaction is the rate determining step as also indicated by Fig. 3 (b).
- $Z_{r_{\text{RWGS}}}$: Increasing the reaction rate constant of the RWGS reaction has negative influence on the DME yield. Here several effects act. Favoring the RWGS produces water, which is also produced in the other two reactions, therefore shifting the equilibrium towards the educt side of all reactions. As can be seen from Eqs. (15) and (16) the increase of $p_{\text{H}_2\text{O}}$ lowers the reaction rate r_{MeOH} which is passed on to the DME production. Moreover, the RWGS consumes the same educts as the MeOH synthesis and therefore negatively weighs on the MeOH production.
- $Z_{r_{\text{DME}}}$: The influence on the yield is negligible, since the DME synthesis step being not rate determining.
- $Z_{D_{\text{N}_2}}$: Mass transfer of Nitrogen has no influence since it is inert.
- $Z_{D_{\text{H}_2}}$: Mass transfer of Hydrogen has negligible influence.
- $Z_{D_{\text{H}_2\text{O}}}$: Increasing the mass transfer rate of water has positive influence on the yield for larger distances. By increasing the transport rate, water is transported away from the inner shell easier. Lowering the H_2O concentration increases the reaction rates of MeOH and the RWGS reactions Eqs. (15) and (16). Although the H_2O concentration at the outer layering catalyst increases Eq. (19) shows that DME production benefits more from an increases MeOH concentration than it is hampered by the presence of H_2O . The effect weighs heavier for larger distances when mass transfer limit occurs.

- $Z_{D_{CO}}$: Increasing the mass transfer rate of CO has a negative effect at larger distances. Being product of the RWGS, the removal from the inner shell due to diffusion is beneficial for the RWGS from equilibrium point of view. Here, the same arguments as for $Z_{r_{RWGS}}$ hold.
- $Z_{D_{H_2}}$: Mass transfer of CO_2 has negligible influence.
- $Z_{D_{MeOH}}$: Increasing the mass transfer rate of MeOH leads to higher yields of DME and MeOH. Favoring the transport from the inner shell where it is produced is beneficial for the MeOH synthesis from equilibrium point of view. Producing more MeOH automatically increases DME production.
- $Z_{D_{DME}}$: Mass transfer of DME has negligible influence.

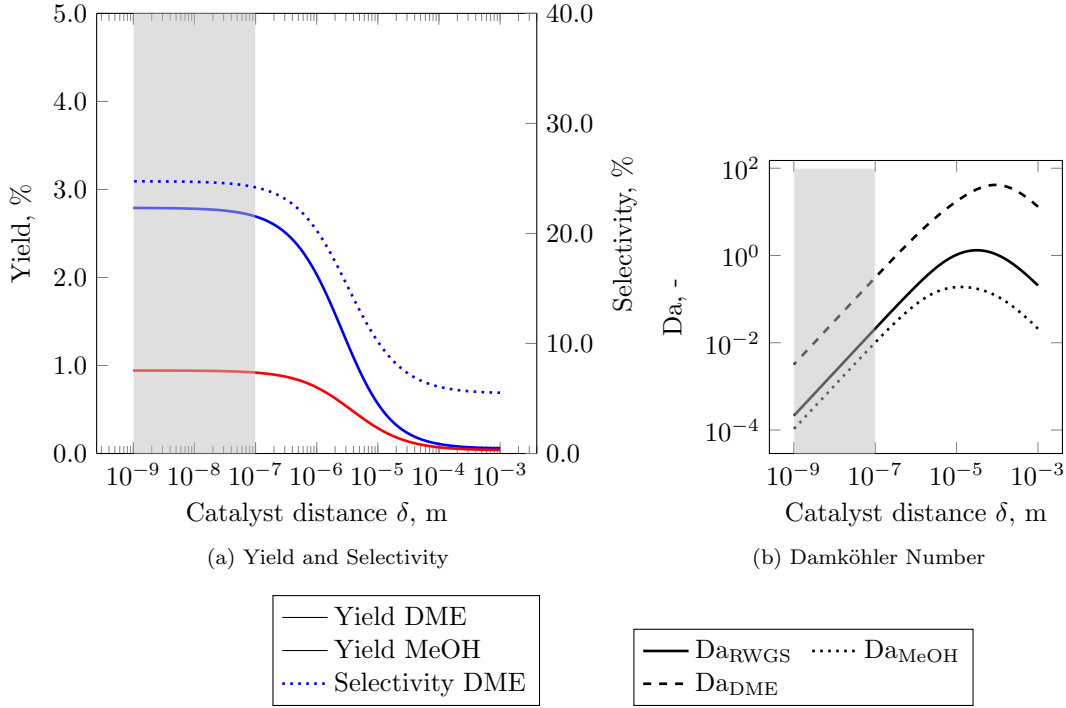


Figure 3: Yield for MeOH and DME (a) (left) and selectivity for DME (a) (right) and Damköhler Numbers (b) plotted against catalyst distance δ for a constant inner radius R_1 showing that 'the closer the better' applies for showcase I

4.2. Case II -Influence of coupling due to catalyst poisoning by adsorption ($k_{0,9} = 0$)

For the second showcase we introduce a back-coupling of the second reaction on the first in order to investigate if that back-coupling changes the result of "the closer the better" from Section 4.1. By damping the reaction rates on the Cu/ZnO catalyst r_i due to adsorption of DME, this case mimics catalyst poisoning. We decided to introduce an extra equation handling the adsorption instead of including it in Eqs. (15)

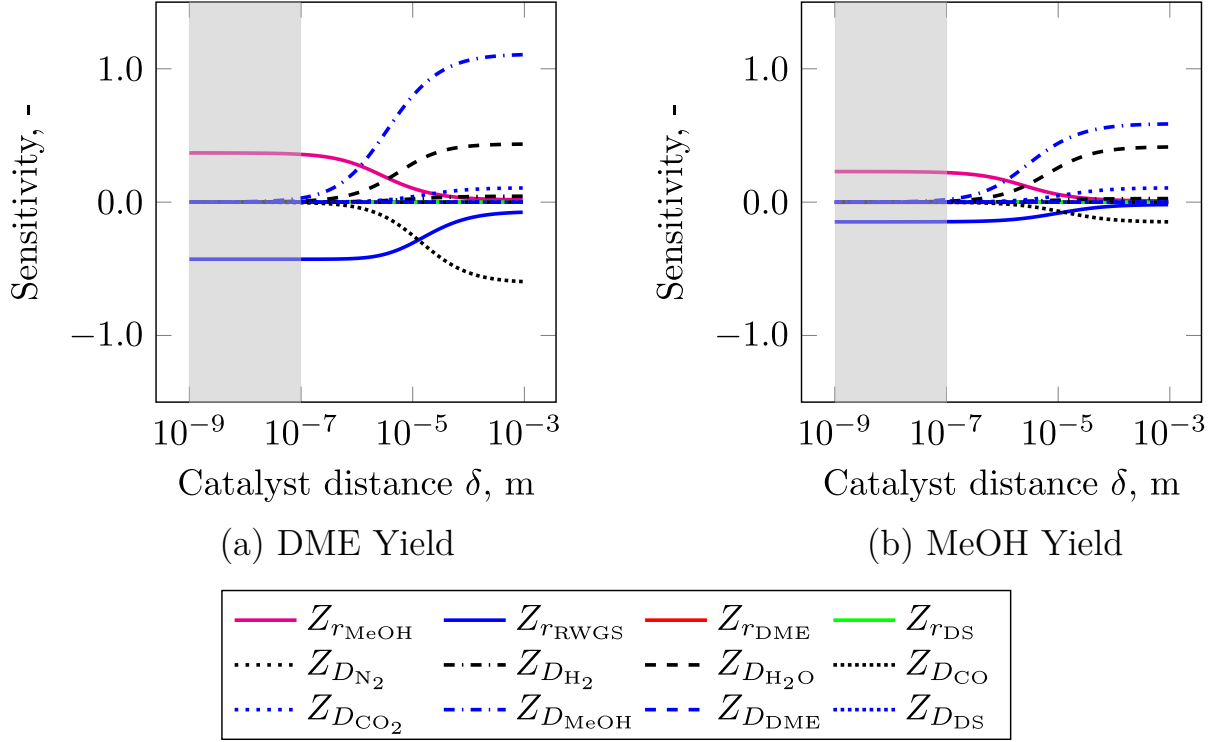


Figure 4: Showcase I: Sensitivities for the yield of species DME (a) and MeOH (b) on Diffusivity coefficients and reaction rate constants plotted against catalyst distance δ for constant inner radius R_1

and (16) to isolate the effect of adsorption in the discussion. Using the Langmuir adsorption with the equilibrium constant K_{DME} for describing the surface coverage Θ a simple equilibrium approach is chosen for analyzing the influence. This model perfectly conserves the number of sites since the coverage Θ is bounded between 0 and 1 and the reaction keeps running on the free sites.

$$\Theta = \frac{K_{\text{DME}} \cdot p_{\text{DME}}}{1 + K_{\text{DME}} \cdot p_{\text{DME}}} \quad (26)$$

$$K_{\text{DME}} = 2 \text{ bar}^{-1} \cdot \exp\left(\frac{20.000 \text{ J mol}^{-1}}{R^{\text{gas}} \cdot T}\right) \quad (27)$$

$$r_l^{\text{Poison}} = r_l \cdot (1 - \Theta) \quad (28)$$

On the left axis of Fig. 6 (a), the yields of DME and MeOH (Eq. (23)) are plotted against the catalyst distance for showcase II. The selectivity towards DME (Eqs. (22) and (24)) is shown on the right axis.

The DME which is transported due to concentration gradient into the inner of the particle adsorbs on the catalytic surface of the methanol synthesis catalyst. As stated in Section 4.1, the reaction rate of MeOH

production is higher for smaller catalyst distance and as a consequence, the DME production is increased resulting in a larger DME concentration at the outer shell. Also, the transport resistance is lower for small catalyst distance, which leads to an increased flux of DME towards the core. These effects lead to a higher DME concentration at the inner shell, which leads to higher adsorption rates and as a consequence the methanol synthesis reaction is inhibited more for lower catalyst distances. So this effect compares to the production of an unwanted side product remaining at the core and deactivating active sites. By this catalyst poisoning, the yields of both MeOH and DME decrease slightly compared to the case without coupling in Fig. 4 (a). The graphs for yield for cases I and II show similar trends, only at different absolute values, whereas the graphs for the selectivity differ significantly. As shown in Fig. 5 (b), the Da of the RWGS and MeOH synthesis reactions cross each other, making the RWGS reaction the rate determining step for smaller distances. Although the yield of DME and MeOH are smaller due to blocking of active sites, an increase in selectivity towards DME is noticeable. Both MeOH synthesis and RWGS reaction are inhibited. With a small distance between the active shells, the system is nowhere near mass transfer limit so that almost all the MeOH is consumed to produce DME without inhibition. Nevertheless, the yield still reaches its maximum for smallest distances so that the statement "the closer the better" still holds. Due to the equilibrium based approach of the coupling, the same mass transfer argumentation from Section 4.1 is valid in steady state, only scaling the reaction relatively due to the adsorption. The sensitivities for the showcase with adsorption are depicted in Fig. 6 (a) and (b) and qualitatively show similar behavior as the sensitivities for the showcase without back-coupling. The adsorption energy employed in Eq. (27) for DME on the catalyst was chosen arbitrarily in order to generally study the possible influence. Anyway, increasing or decreasing that value only scales the coverage Θ up and down.

4.3. Case III - Influence of coupling due to reaction of DME on methanol catalyst ($K_{0,8} = 0$)

The third showcase depicts a back-coupling due to a side reaction of the DME to an unwanted Dummy Species DS, which is motivated from a possible reaction to Alkenes [29]. With a simple first order kinetics describing the reaction rate r_{DS} , we introduced a non-equilibrium back-coupling for discussing the influence. For simplicity, the Dummy species has the same thermodynamic properties as DME, so no heat is generated from this reaction and mass is conserved easily.

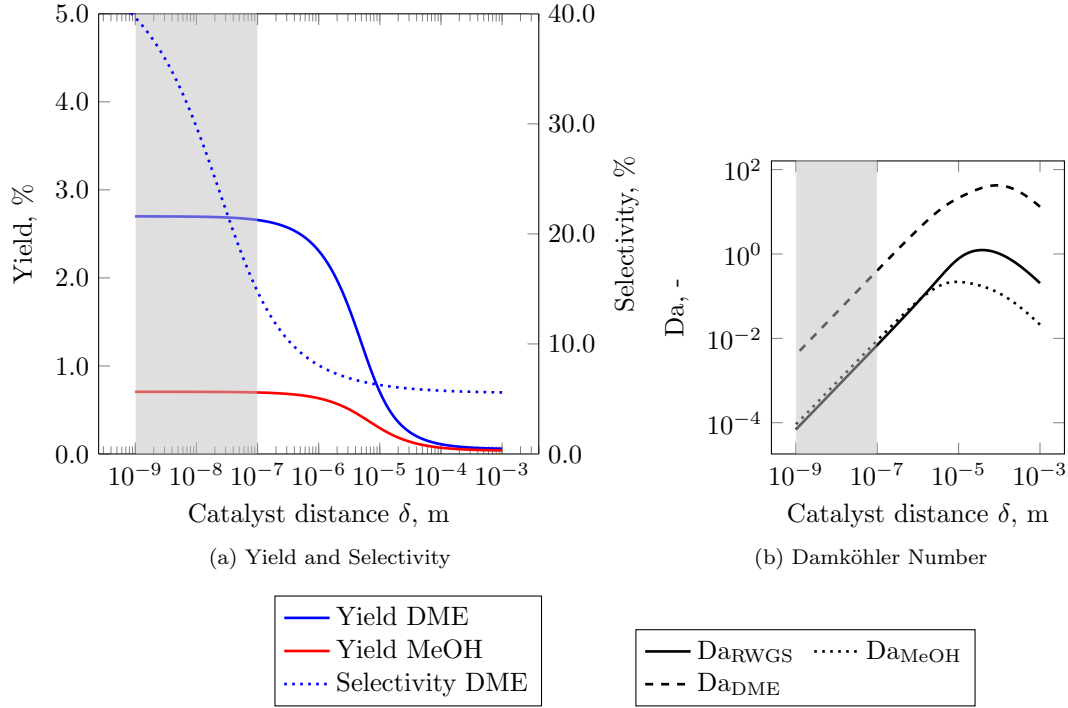


Figure 5: Yield for MeOH and DME (a) (left) and selectivity for DME (a) (right) and Damköhler Numbers (b) plotted against catalyst distance δ for a constant inner radius R_1 indicating that 'the closer the better' applies for showcase II

$$r_{DS} = k_9 \cdot p_{DME} \quad (29)$$

$$k_9 = 1 \times 10^5 \text{ mol kg}_{\text{cat}}^{-1} \text{ s}^{-1} \text{ bar}^{-1} \cdot \exp\left(\frac{-50.000 \text{ J mol}^{-1}}{R^{\text{gas}} \cdot T}\right) \quad (30)$$

In Fig. 7 (a) the yield for DME and MeOH are again plotted against the catalyst distance on the left axis. The selectivity towards DME is shown on the right axis. We can see that allowing for a reaction of DME to some unwanted component on the MeOH synthesis catalyst we obtain a profile with a maximum yield at an optimal catalyst distance. The optimum distance is marked by the black dotted line.

In Fig. 7 (b) the Damköhler Numbers for the reactions employed in showcase III are plotted against the catalyst distance. A short distance between the catalytic shells results in a small transport resistance for all species, so that the educt species for the MeOH reaction are transported easily to the inner shell and the MeOH on the other hand is easily transported to the outer shell where it reacts towards DME. The Da of the four reactions show different sensitivities on the distance of the catalysts, depending on their kinetics. The optimal distance for the DME yield is located at the point where $Da_{DS} = Da_{DME}$. The sensitivities of

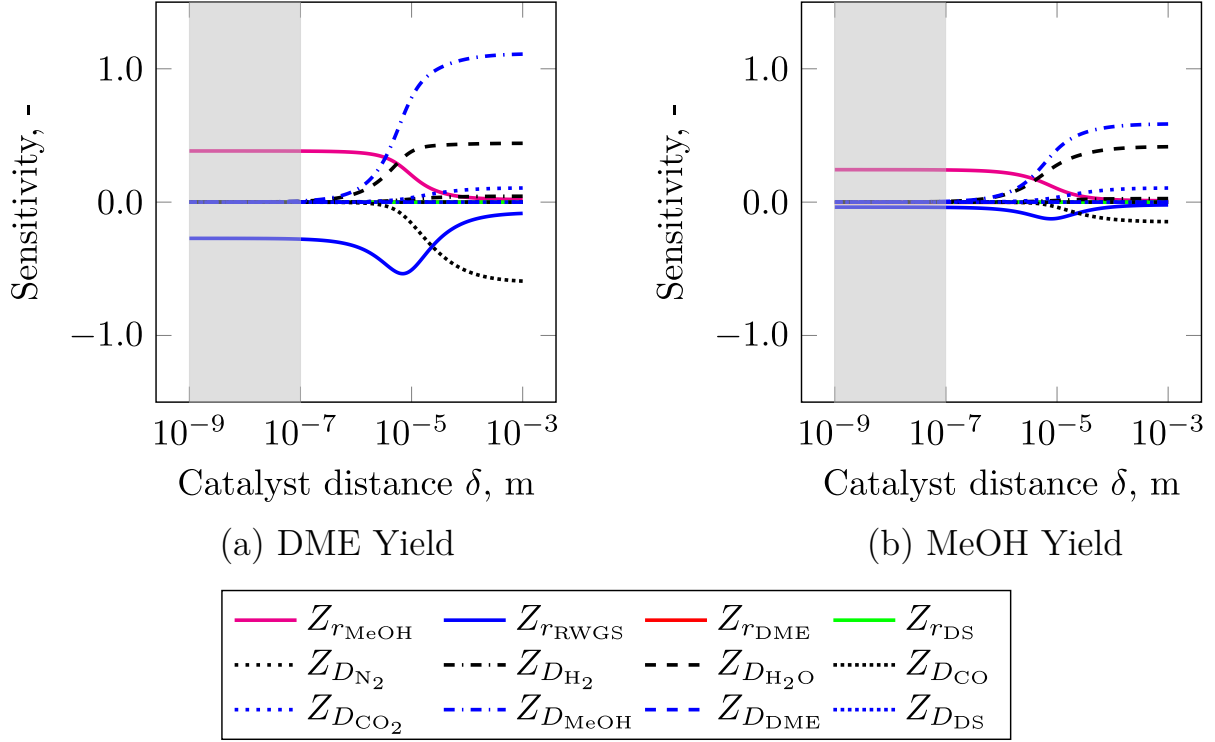


Figure 6: Showcase II: Sensitivities for the yield of species DME (a) and MeOH (b) on Diffusivity coefficients and reaction rate constants plotted against catalyst distance δ for constant inner radius R_1

the yields of DME and DS on diffusivities and reaction rates are depicted in Fig. 8. The influence for most parameters is qualitatively still the same as for the showcases discussed before except for:

- $Z_{r_{\text{DS}}}$: The reaction rate towards DS has negative impact on the DME yield for very close distance of the catalysts. For larger distances the transport resistance in the particle ensures the DME to be transported to the surrounding gas phase rather than to the inner of the particle.
- $Z_{D_{\text{DME}}}$: By increasing the diffusivity of DME, the yield of DS increases as well since more of the valued component is transported to the inner of the particle where it reacts to DS instead of being transported into the bulk phase outside of the particle. The closer the catalysts are, the less severe this effect gets since the transport resistance in the particle is lower from the beginning. On the other hand, the negative impact on the yield of DME behaves just the other way around. For longer distances between the catalysts, the DME yield is less sensitive on the diffusivity than for smaller distances. This can be explained by taking a closer look at Eq. (19), where the partial pressure of DME weighs negatively on the reaction rate. This means that a removal of DME enhances the production additionally to shifting

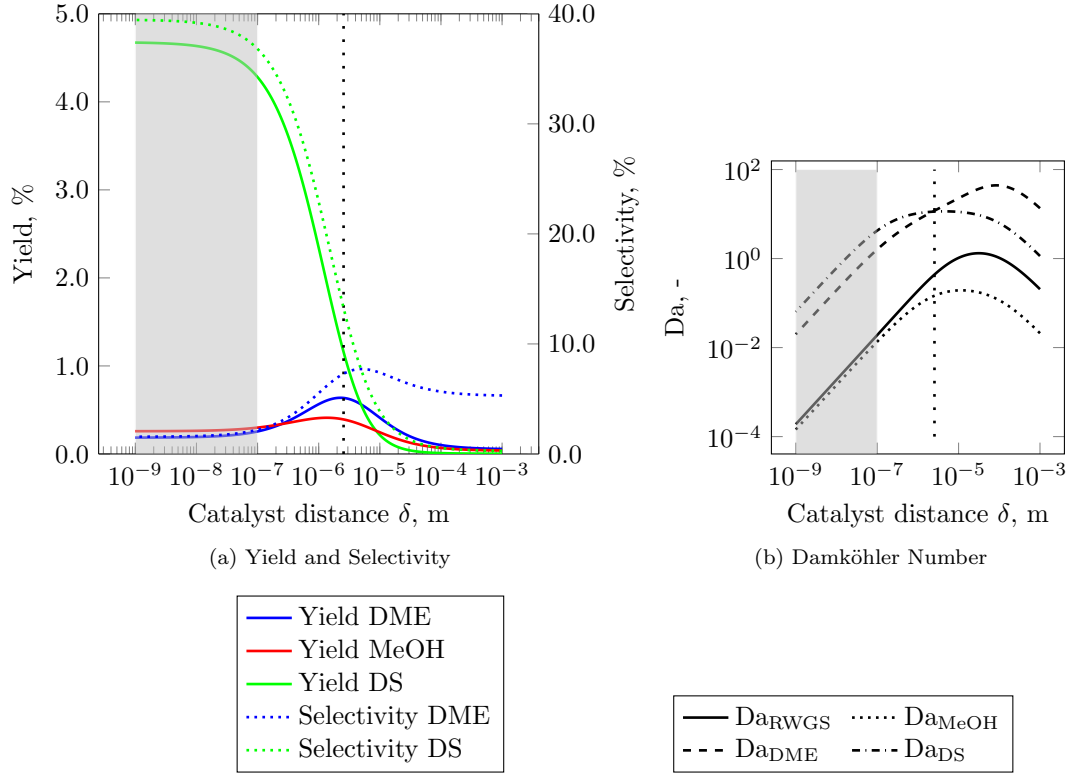


Figure 7: Yield for MeOH and DME (a) (left) and selectivity for DME (a) (right) plotted against catalyst distance for constant inner radius R_1 for showcase III - coupling due to DME consuming side reaction. Damköhler Numbers (b) plotted against catalyst distance δ for a constant inner radius R_1 showing a distinct maximum yield for DME due to backcoupling at the point where $Da_{DS} = Da_{DME}$

the equilibrium term in the equation. Thereby, the enhancement counteracts the consumption towards DS for larger distances. For smaller catalyst distances, the transport resistance is lower so that more molecules of DME are transported to the core where they are consumed to DS. From Fig. 7 (b) we see that here $Da_{DS} > Da_{DME}$ so that almost all produced DME is consumed to DS.

- $Z_{D_{DS}}$: Mass transfer of DS has negligible influence in this showcase due to the simple 1st order kinetics without adsorption or equilibrium term. With Eq. (29) DME is converted towards DS no matter what the DS concentration is. Moreover, molecules of DS are assumed to not have influence on any other reaction rate and therefore its transport will not effect other reaction rates.

Remarkably, the discussed effects due to backcoupling only occur for smaller distances between the catalytically active layers. For the largest distance in our simulations of 1×10^{-3} m, we can observe more or less the same values for yield and selectivity in all presented cases. Moreover, the sensitivities do not significantly change when backcoupling is introduced except for the newly added parameter r_{DS} and the

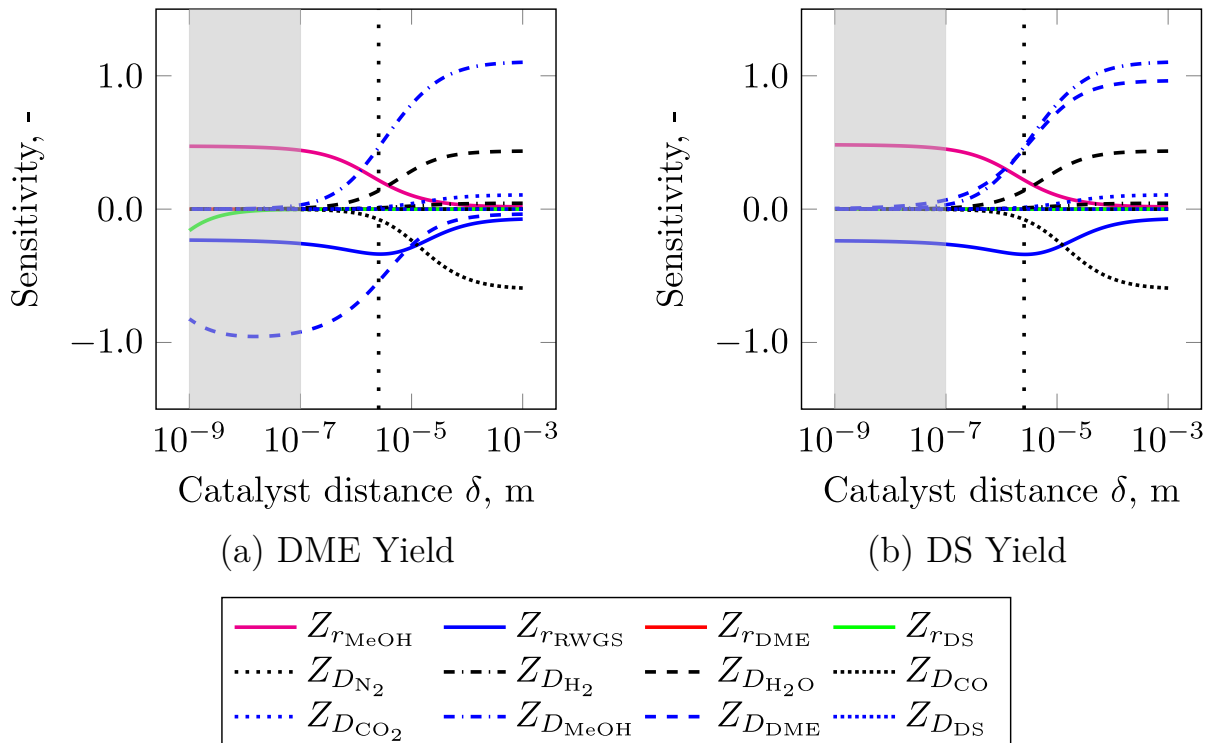


Figure 8: Showcase III: Sensitivities for the yield of species: (a) DME and (b) DS on Diffusivity coefficients and reaction rate constants plotted against catalyst distance δ for constant inner radius R_1

transport parameter for DME D_{DME} . The effects are strongest, where the transition from kinetic limit to mass transfer limit occurs. For larger distances, the sensitivities regarding r_{DS} and D_{DME} vanish. Here, yield and selectivity converge to the solution of the uncoupled case.

5. Conclusions

In this article, we presented a novel, simple and computationally efficient approach to modeling core-shell catalyst particles in order to investigate the influence of the distance between catalytically active sites. The model was developed by model reduction of the balances of the conserved quantities mass and energy. Exploiting geometrical symmetry and other justified simplifications the model was reduced from a system of partial differential equations to a small system of algebraic equations. Thereby the computational effort decreased enormously, enabling quick solution on a workstation instead of needing super computers.

Employing the sequential heterogeneously catalyzed reactions from CO_2 to methanol and methanol to DME as an example case study, we presented three showcases with increasing complexity regarding back-coupling between the active catalyst particle shells. The Reverse Water Gas Shift reaction was additionally

considered as a side reaction.

As a benchmark, a case without back-coupling was introduced showing the dependency of yield and selectivity towards DME, the product of the second reaction, for varying distance between core and shell. In case I, both yield and selectivity showed highest values for the lowest distance. In case II it showed that adding an equilibrium based adsorption mechanism based on Langmuir adsorption on the core in order to represent catalyst poisoning of the first catalyst by the product of the second reaction decreased yield and increased selectivity for small distances of the catalytic layers. For larger distances the influence was negligible. Nevertheless, highest values were analogically to the benchmark case found at the closest distance between core and shell. Case III demonstrated the case where the DME is consumed to a dummy species on the methanol synthesis catalyst. We introduced a first order kinetics taking place on the core. In this case, we observed a non-zero maximum for yield and selectivity, located at the point where $Da_{DS} = Da_{DME}$. Interestingly, the influence of the introduced backcoupling was again negligible at larger distances.

The answer of the system showed high sensitivity on the reaction rate of the methanol synthesis for small distances. On the other hand, the system answer was transport dominated for larger distances.

Overall we could observe that the validity of the assumption "the closer the better" very much depends on the case and the circumstances we look at. In our study the assumption is valid for the conditions without backcoupling or with equilibrium based backcoupling. On the other hand, for non-equilibrium based backcoupling the assumption loses its validity and an optimal non-zero distance is observed. In real systems some sort of backcoupling is highly likely. The optimal distance can therefore not a priori be deduced. Rather, it depends on the detailed interplay of meso- and macroscale transport and kinetics and must be determined by a careful analysis taking these effects into account. Furthermore, our results indicate that the performance might sensitively depend on the distance. Therefore, the control of the distance is crucial for developing optimal catalytic systems.

Moreover, in real systems other effects such as ion-migration [8] might occur which was not addressed in the scope of this study but might be implemented in the near future.

6. Acknowledgements

Funded by the Deutsche Forschungsgemeinschaft (DFG, German Research Foundation) under Germany's Excellence Strategy – EXC 2008 – 390540038 – UniSysCat and by the CRC 1114 "Scaling Cascades in Complex Systems" funded by the Deutsche Forschungsgemeinschaft (project ID: 235221301). Gefördert durch die Deutsche Forschungsgemeinschaft (DFG) im Rahmen der Exzellenzstrategie des Bundes und der

Länder – EXC 2008/1 – 390540038 – UniSysCat und beim CRC 1114 “Scaling Cascades in Complex Systems” gefördert durch die Deutsche Forschungsgemeinschaft (project ID: 235221301).

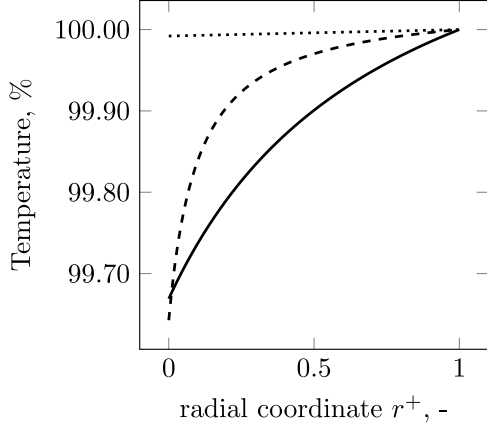
References

- [1] C. M. Friend, B. Xu, Heterogeneous catalysis: A central science for a sustainable future, *Accounts of Chemical Research* 50 (3) (2017) 517–521. doi:10.1021/acs.accounts.6b00510.
- [2] J. Wei, Q. Ge, R. Yao, Z. Wen, C. Fang, L. Guo, H. Xu, J. Sun, Directly converting CO₂ into a gasoline fuel, *Nature Communications* 8 (1) (may 2017). doi:10.1038/ncomms15174.
- [3] B. Donoeva, K. P. de Jong, Torn between two sites, *Nature Materials* 19 (1) (2019) 5–6. doi:10.1038/s41563-019-0568-0.
- [4] P. B. Weisz, Polyfunctional heterogeneous catalysis, in: *Advances in Catalysis*, Elsevier, 1962, pp. 137–190. doi:10.1016/s0360-0564(08)60287-4.
- [5] J. Francis, E. Guillon, N. Bats, C. Pichon, A. Corma, L. Simon, Design of improved hydrocracking catalysts by increasing the proximity between acid and metallic sites, *Applied Catalysis A: General* 409-410 (2011) 140–147. doi:10.1016/j.apcata.2011.09.040.
- [6] J. Kim, W. Kim, Y. Seo, J.-C. Kim, R. Ryoo, n-heptane hydroisomerization over pt/MFI zeolite nanosheets: Effects of zeolite crystal thickness and platinum location, *Journal of Catalysis* 301 (2013) 187–197. doi:10.1016/j.jcat.2013.02.015.
- [7] J. Zecevic, G. Vanbutsele, K. P. de Jong, J. A. Martens, Nanoscale intimacy in bifunctional catalysts for selective conversion of hydrocarbons, *Nature* 528 (7581) (2015) 245–248. doi:10.1038/nature16173.
- [8] Y. Wang, G. Wang, L. I. Wal, K. Cheng, Q. Zhang, K. P. Jong, Y. Wang, Visualizing element migration over bifunctional metal-zeolite catalysts and its impact on catalysis, *Angewandte Chemie International Edition* (jun 2021). doi:10.1002/anie.202107264.
- [9] Y. Wang, W. Wang, Y. Chen, J. Ma, R. Li, Synthesis of dimethyl ether from syngas over core-shell structure catalyst cuo-zno-al₂o₃@sio₂-al₂o₃, *Chemical Engineering Journal* 250 (2014) 248 – 256. doi:https://doi.org/10.1016/j.cej.2014.04.018.
URL <http://www.sciencedirect.com/science/article/pii/S138589471400446X>
- [10] G. Yang, N. Tsubaki, J. Shamoto, Y. Yoneyama, Y. Zhang, Confinement effect and synergistic function of h-zsm-5/cu-zno-al₂o₃ capsule catalyst for one-step controlled synthesis, *Journal of the American Chemical Society* 132 (23) (2010) 8129–8136. doi:10.1021/ja101882a.
URL <https://doi.org/10.1021/ja101882a>
- [11] S. Das, J. Pérez-Ramírez, J. Gong, N. Dewangan, K. Hidajat, B. C. Gates, S. Kawi, Core-shell structured catalysts for thermocatalytic, photocatalytic, and electrocatalytic conversion of co₂, *Chem. Soc. Rev.* 49 (2020) 2937–3004. doi:10.1039/C9CS00713J.
URL <http://dx.doi.org/10.1039/C9CS00713J>
- [12] A. Thomas, Much ado about nothing – a decade of porous materials research, *Nature Communications* 11 (12 2020). doi:10.1038/s41467-020-18746-5.
- [13] E. Gioria, L. Duarte-Correa, N. Bashiri, W. Hetaba, R. Schomaecker, A. Thomas, Rational design of tandem catalysts using a core-shell structure approach, *Nanoscale Adv.* 3 (12) (2021) 3454–3459. doi:10.1039/d1na00310k.

- [14] W. Ding, M. Klumpp, S. Lee, S. Reuß, S. A. Al-Thabaiti, P. Pfeifer, W. Schwieger, R. Dittmeyer, Simulation of one-stage dimethyl ether synthesis over a core-shell catalyst, *Chemie Ingenieur Technik* 87 (6) (2015) 702–712. [arXiv:https://onlinelibrary.wiley.com/doi/pdf/10.1002/cite.201400157](https://onlinelibrary.wiley.com/doi/pdf/10.1002/cite.201400157), [doi:https://doi.org/10.1002/cite.201400157](https://doi.org/10.1002/cite.201400157).
URL <https://onlinelibrary.wiley.com/doi/abs/10.1002/cite.201400157>
- [15] E. S. Van-Dal, C. Bouallou, Design and simulation of a methanol production plant from co₂ hydrogenation, *Journal of Cleaner Production* 57 (2013) 38 – 45. [doi:https://doi.org/10.1016/j.jclepro.2013.06.008](https://doi.org/10.1016/j.jclepro.2013.06.008).
- [16] K.-S. Ha, Y.-J. Lee, J. W. Bae, Y. W. Kim, M. H. Woo, H.-S. Kim, M.-J. Park, K.-W. Jun, New reaction pathways and kinetic parameter estimation for methanol dehydration over modified zsm-5 catalysts, *Applied Catalysis A: General* 395 (1) (2011) 95 – 106. [doi:https://doi.org/10.1016/j.apcata.2011.01.025](https://doi.org/10.1016/j.apcata.2011.01.025).
- [17] F. Kapteijn, J. A. Moulijn, *Laboratory Catalytic Reactors: Aspects of Catalyst Testing 1 A list of symbols used in the text is provided at the end of the chapter.*, American Cancer Society, 2008, Ch. 9.1, pp. 2019–2045. [arXiv:https://onlinelibrary.wiley.com/doi/pdf/10.1002/9783527610044.hetcat0108](https://onlinelibrary.wiley.com/doi/pdf/10.1002/9783527610044.hetcat0108), [doi:https://doi.org/10.1002/9783527610044.hetcat0108](https://doi.org/10.1002/9783527610044.hetcat0108).
URL <https://onlinelibrary.wiley.com/doi/abs/10.1002/9783527610044.hetcat0108>
- [18] J. E. Sutton, J. M. Lorenzi, J. T. Krogel, Q. Xiong, S. Pannala, S. Matera, A. Savara, Electrons to reactors multiscale modeling: Catalytic co oxidation over ruo₂, *ACS Catal.* 8 (2018) 5002–5016.
- [19] I. Müller, *Thermodynamics*, Pitman, Boston, 1985.
- [20] O. Deutschmann, *Computational Fluid Dynamics Simulation of Catalytic Reactors*, American Cancer Society, 2008, Ch. 6.6, pp. 1811–1828. [arXiv:https://onlinelibrary.wiley.com/doi/pdf/10.1002/9783527610044.hetcat0097](https://onlinelibrary.wiley.com/doi/pdf/10.1002/9783527610044.hetcat0097), [doi:https://doi.org/10.1002/9783527610044.hetcat0097](https://doi.org/10.1002/9783527610044.hetcat0097).
URL <https://onlinelibrary.wiley.com/doi/abs/10.1002/9783527610044.hetcat0097>
- [21] M. Sinstein, C. Scheurer, S. Matera, V. Blum, K. Reuter, H. Oberhofer, Efficient implicit solvation method for full potential DFT, *Journal of Chemical Theory and Computation* 13 (11) (2017) 5582–5603. [doi:10.1021/acs.jctc.7b00297](https://doi.org/10.1021/acs.jctc.7b00297).
- [22] T. Maffei, G. Gentile, S. Rebughini, M. Bracconi, F. Manelli, S. Lipp, A. Cuoci, M. Maestri, A multiregion operator-splitting CFD approach for coupling microkinetic modeling with internal porous transport in heterogeneous catalytic reactors, *Chemical Engineering Journal* 283 (2016) 1392–1404. [doi:10.1016/j.cej.2015.08.080](https://doi.org/10.1016/j.cej.2015.08.080).
- [23] G. Tolsdorf, E. Esche, G. Wozny, J.-U. Repke, Customized code generation based on user specifications for simulation and optimization, *Computers & Chemical Engineering* 121 (2019) 670 – 684. [doi:https://doi.org/10.1016/j.compchemeng.2018.12.006](https://doi.org/10.1016/j.compchemeng.2018.12.006).
- [24] K. Bussche, G. Froment, A steady-state kinetic model for methanol synthesis and the water gas shift reaction on a commercial cu/zno/al₂o₃catalyst, *Journal of Catalysis* 161 (1) (1996) 1 – 10. [doi:https://doi.org/10.1006/jcat.1996.0156](https://doi.org/10.1006/jcat.1996.0156).
- [25] G. Graaf, P. Sijtsema, E. Stamhuis, G. Joosten, Chemical equilibria in methanol synthesis, *Chemical Engineering Science* 41 (11) (1986) 2883 – 2890. [doi:https://doi.org/10.1016/0009-2509\(86\)80019-7](https://doi.org/10.1016/0009-2509(86)80019-7).
- [26] G. Chinchén, P. Denny, D. Parker, M. Spencer, D. Whan, Mechanism of methanol synthesis from co₂/co/h₂ mixtures over copper/zinc oxide/alumina catalysts: use of¹⁴C-labelled reactants, *Applied Catalysis* 30 (2) (1987) 333 – 338. [doi:https://doi.org/10.1016/S0166-9834\(00\)84123-8](https://doi.org/10.1016/S0166-9834(00)84123-8).
- [27] A. Y. Rozovskii, Modern problems in the synthesis of methanol, *Russian Chemical Reviews* 58 (1) (1989) 41–56. [doi:10.1070/rc1989v058n01abeh003425](https://doi.org/10.1070/rc1989v058n01abeh003425).

- [28] W.-Z. Lu, L.-H. Teng, W.-D. Xiao, Simulation and experiment study of dimethyl ether synthesis from syngas in a fluidized-bed reactor, *Chemical Engineering Science* 59 (22) (2004) 5455 – 5464, iSCRE18. doi:<https://doi.org/10.1016/j.ces.2004.07.031>.
- [29] S. C. Aslanov, A. Q. Buxorov, N. I. Fayzullayev, Catalytic synthesis of c2-c4-alkenes from dimethyl ether, *International Journal of Engineering Trends and Technology* 69 (4) (2021) 67–75. doi:10.14445/22315381/ijett-v69i4p210.
- [30] C. T. Campbell, The degree of rate control: A powerful tool for catalysis research, *ACS Catalysis* 7 (4) (2017) 2770–2779. doi:10.1021/acscatal.7b00115.

Appendix A. Temperature profile



--- $\delta = 1000 \mu\text{m}$ — $\delta = 133.5 \mu\text{m}$ $\delta = 0.5 \mu\text{m}$

Figure A.9: Normalized temperature profiles over dimensionless radial coordinate for case I and varying active site distance

Appendix B. Sensitivity analysis

The system of governing equations (1) - (10) and (14) can abstractly be written as

$$\sum_q \alpha_q F_q[z] = 0 \quad (\text{B.1})$$

where z is the desired solution, i.e. concentrations and temperature in the particle and the surrounding gas phase. The nonlinear mappings $F_q[z]$ represent either the terms describing the diffusion of a certain species in a particular subdomain, i.e. those terms in eqn. (1), - (10) and (14) carrying the respective diffusion coefficient, or those terms associated with a certain turnover frequency function $r_l(*)$, or the total mass flux $F^{\text{kg,in}}$, or continuity conditions. For performing sensitivity analysis, we have introduced the parameters α_q to alter the influence of each physical aspect and $\alpha_q = 1$ means that we consider our original set of governing equations. Now, each term $F_q[z]$ except the continuity conditions represents some abstract kind of rate and if increase α_q we accelerate the respective physical process. For instance, if $F_q[z]$ represents a diffusion, increasing α_q results in faster diffusion. We want to note, that the continuity conditions being no rates is unproblematic, because the sensitivity with respect to them is zero anyways.

Any derived quantity $G[z]$, in our case the yield, is then a function of the parameters α_q , when eq. (B.1)

has a unique solution and z is this solution. We define our sensitivities as

$$Z_q := \left(\frac{1}{G} \frac{\partial G}{\partial \alpha_q} \right)_{\alpha_{q'} \neq q} \quad (\underline{\alpha} = 1) \quad (\text{B.2})$$

where $\underline{\alpha} = 1$ means that we evaluate the partial derivative for all α_q set to one. This definition of the sensitivity is in complete analogy to the Degree of Rate Control[30]. If eq. (B.1) would be a set of steady state microkinetic equations, G a turnover frequency and $F_q[z]$ would represent the effect of an elementary step and its inverse, Z_q would simply be the Degree of Rate Control of that reaction. For our purposes, the above definition has the advantage that we treat all different phenomena - reaction, transport and flow - on the same footing and thus the sensitivities are comparable. The sensitivities discussed in Section 4 were calculated by finite differences of the yield Y conducting simulations for $\alpha = 1$ and $\alpha = 1.01$.

$$Z := \frac{\partial Y}{\partial \alpha} \cdot \frac{1}{Y} \approx \frac{Y_{\alpha=1} - Y_{\alpha=1.01}}{0.01} \cdot \frac{1}{Y_{\alpha=1}} \quad (\text{B.3})$$

Appendix C. Kinetic Parameters

Table C.2: Kinetic parameters of reaction and adsorption rates used in the simulations with values taken from [15, 16]

Parameter	value	unit	Parameter	value	unit
$k_{0,1}$	1.07	$\text{mol kg}_{\text{cat}}^{-1} \text{s}^{-1} \text{bar}^{-2}$	$E_1^{\text{act.}}$	40,000	J mol^{-1}
$K_{0,2}$	3453.38	-	$E_2^{\text{reac.}}$	0	J mol^{-1}
$K_{0,3}$	0.499	$\text{bar}^{-0.5}$	$E_3^{\text{reac.}}$	17,197	J mol^{-1}
$K_{0,4}$	6.62×10^{-11}	bar^{-1}	$E_4^{\text{reac.}}$	124,119	J mol^{-1}
$k_{0,5}$	1.22×10^{10}	$\text{mol kg}_{\text{cat}}^{-1} \text{s}^{-1} \text{bar}^{-1}$	$E_5^{\text{act.}}$	-98,084	J mol^{-1}
$k_{0,6}$	85,190	$\text{mol kg}_{\text{cat}}^{-1} \text{s}^{-1}$	$E_6^{\text{act.}}$	-55,060	J mol^{-1}
$K_{0,7}$	223.2	bar^{-1}	$E_7^{\text{reac.}}$	105,100	J mol^{-1}
$K_{0,8}$	0.5498	bar^{-1}	$E_8^{\text{reac.}}$	92,000	J mol^{-1}
$k_{0,9}$	1×10^5	$\text{mol kg}_{\text{cat}}^{-1} \text{s}^{-1} \text{bar}^{-1}$	$E_9^{\text{act.}}$	-50,000	J mol^{-1}